



CHORUS

This is the accepted manuscript made available via CHORUS. The article has been published as:

Multiphoton dissociation of $\text{HeH}^{\{+\}}$ below the $\text{He}^{\{+\}}(1s)+\text{H}(1s)$ threshold

D. Ursrey, F. Anis, and B. D. Esry

Phys. Rev. A **85**, 023429 — Published 29 February 2012

DOI: [10.1103/PhysRevA.85.023429](https://doi.org/10.1103/PhysRevA.85.023429)

Multiphoton Dissociation of HeH^+ below the $\text{He}^+(1s) + \text{H}(1s)$ Threshold

D. Ursrey, F. Anis, and B. D. Esry

J.R. Macdonald Laboratory, Kansas State University, Manhattan, Kansas 66506

We discuss the strong-field dynamics of HeH^+ , the simplest stable heteronuclear molecule, focusing on identifying a laser regime for which there is a sufficient dissociation signal for experimental measurement. We numerically solve the time-dependent Schrödinger equation to obtain total dissociation probabilities, kinetic energy release spectra, and momentum distributions for wavelengths from 800 nm to 2400 nm. The suitability of this simple system as a prototype for understanding the strong-field nuclear dynamics of heteronuclear dissociation is discussed.

I. INTRODUCTION

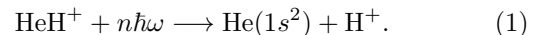
There is considerable interest in the dynamics of molecules in intense laser fields [1–4]. Being the simplest molecules, H_2^+ and D_2^+ have been at the center of many of these studies. Their simplicity allows for theoretical studies with minimal approximations [1, 5–11], while the accuracy of these calculations opens the possibility for quantitative comparison with experimental results [5, 6]. Because of these features, H_2^+ and D_2^+ serve as benchmark systems, providing insight into how more complicated molecules behave in intense laser fields.

In these benchmark studies of H_2^+ and its isotopes, many interesting phenomena have been calculated and measured. Among these are above threshold dissociation [12], below threshold dissociation [13], coherent control of dissociation through variation of carrier envelope phase of a single color pulse [14–16] or the delay between two pulses with different colors [17–19], and bond softening [20–22]. Given the utility and success of these H_2^+ studies, a natural next step is to identify and study a similarly fundamental heteronuclear system. Carrying out calculations on such a system will not only provide additional insight into how the aforementioned phenomena generalize, but it will also allow for the identification of new phenomena that are not present in homonuclear molecules. We exclude the simplest heteronuclear molecule, HD^+ , because it does not produce an electronic asymmetry within the usual infinite nuclear mass Born-Oppenheimer approximation.

Thus, we propose HeH^+ as a benchmark system for studying the nuclear response of heteronuclear molecules to intense laser fields. The viability of this species as an experimental target has already been established. Specifically, ion beams of HeH^+ have been produced to demonstrate the existence of metastable HeH^{2+} [23, 24] and, more recently, to serve as targets for an ultraviolet free-electron laser [25]. In this paper, we will focus on dissociation of HeH^+ at far- to mid-infrared wavelengths between 800 nm and 2400 nm. Intense, short pulses with such long wavelengths are becoming increasingly available experimentally and have been used in recent years to study high harmonic generation [26] and ionization [27, 28]. We will limit our exploration to five and ten cycle laser pulses with intensities between 10^{12} W/cm² and 10^{14} W/cm². Our results show that although the

dissociation probability under these conditions is small for the more standard 800 nm pulses, the longer wavelengths in our parameter space are capable of producing substantial dissociation, making this process experimentally accessible.

We argue that the large difference in energy between the ground and first excited electronic channels for HeH^+ causes permanent dipole transitions to be much more probable than electronic excitation for the wavelengths considered. Thus, for the laser parameters studied, we consider only dissociation to the lowest channel, *i.e.*,



Because the system is dominated by single channel effects, it behaves analogously to an atom in a laser field. This atom-like behavior allows us to understand physical observables calculated for HeH^+ using pictures previously developed to study intense field ionization. Moreover, it opens up interesting opportunities to observe phenomena usually associated with atoms in a molecular system.

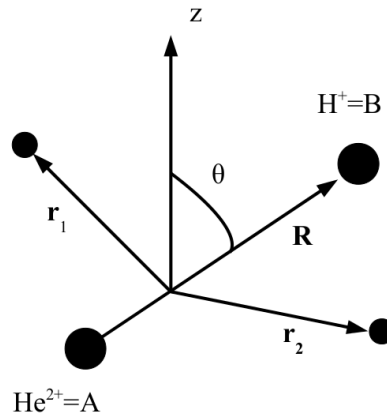


FIG. 1. Coordinates used in the Hamiltonian.

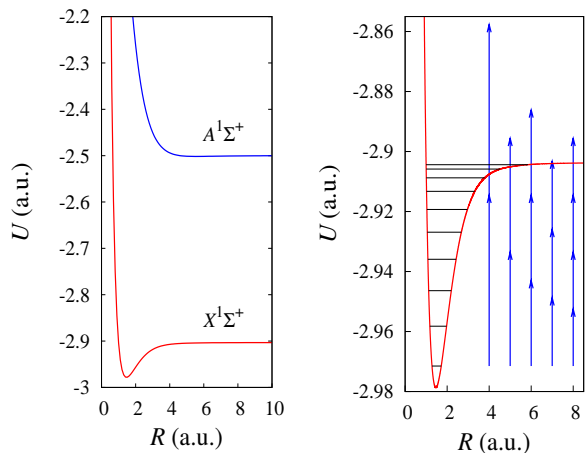


FIG. 2. (Color online.) (a) The adiabatic potential energy curves [29] for the ground state of HeH^+ , $X^1\Sigma^+$, and the first excited singlet state, $A^1\Sigma^+$. (b) The $X^1\Sigma^+$ potential used in our calculations [30] plotted along with the vibrational levels for zero orbital angular momentum. The arrows indicate the energy after dissociation from the absorption of 800 nm, 1200 nm, 1600 nm, 2000 nm, and 2400 nm (from left to right) photons from the vibrational ground state.

II. THEORETICAL METHODS

A. Schrödinger Equation in the Single Channel Approximation

All calculations in this paper use atomic units and are carried out by solving the time-dependent Schrödinger equation in the Born-Oppenheimer approximation. We treat the laser's electric field classically and use the length gauge within the dipole approximation. Using the dipole operator

$$\mathbf{d} = -\left(\frac{3 + m_A + m_B}{2 + m_A + m_B}\right)(\mathbf{r}_1 + \mathbf{r}_2) + \left(\frac{m_A - 2m_B}{m_A + m_B}\right)\mathbf{R}, \quad (2)$$

the time-dependent Schrödinger equation is given by

$$i\frac{\partial}{\partial t}\Psi = \left[-\frac{1}{2\mu_{AB}}\nabla_{\mathbf{R}}^2 + H_{\text{el}} - \mathcal{E}(t) \cdot \mathbf{d}\right]\Psi, \quad (3)$$

where H_{el} is the electronic part of the Hamiltonian including nuclear repulsion and \mathcal{E} is the electric field produced by the incident laser pulse. In Eq. (3), the coordinates are as shown in Fig. 1, and the reduced mass is given by

$$\frac{1}{\mu_{AB}} = \frac{1}{m_A} + \frac{1}{m_B}. \quad (4)$$

The Born-Oppenheimer potentials and electronic wavefunctions are found by solving

$$H_{\text{el}}\Phi_{\nu\Lambda}(R; \mathbf{r}_1, \mathbf{r}_2) = U_{\nu\Lambda}(R)\Phi_{\nu\Lambda}(R; \mathbf{r}_1, \mathbf{r}_2). \quad (5)$$

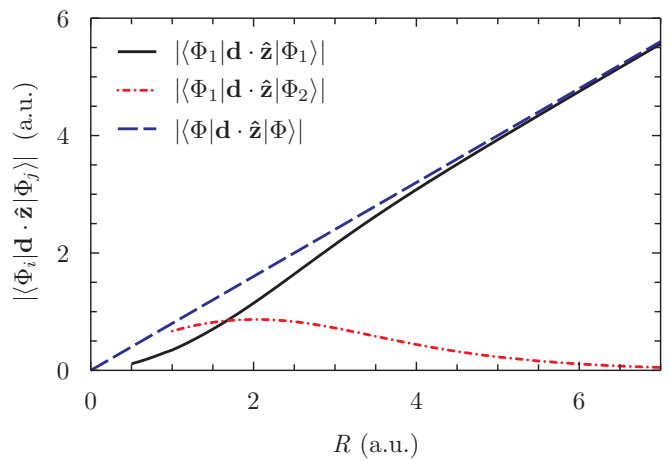


FIG. 3. (Color online.) The body frame z -axis projection of the $X^1\Sigma^+$ permanent dipole, $\langle\Phi_1|\mathbf{d}|\Phi_1\rangle$, and $X^1\Sigma^+-A^1\Sigma^+$ transition dipole, $\langle\Phi_1|\mathbf{d}|\Phi_2\rangle$, from Ref. [29] along with our approximate permanent dipole $\langle\Phi|\mathbf{d}|\Phi\rangle$ from Eq. (7).

In this paper, we use the potentials from Ref. [30]. Because $\Phi_{\nu\Lambda}(R; \mathbf{r}_1, \mathbf{r}_2)$ form a complete set in the electronic coordinates, we can write

$$\Psi = \sum_{J\alpha\Lambda M} \frac{1}{R} F_{J\alpha\Lambda}(R, t) \tilde{D}_{M\Lambda}^J(\phi, \theta, 0) \Phi_{\alpha\Lambda}(R; \mathbf{r}_1, \mathbf{r}_2), \quad (6)$$

where α denotes the electronic state, Λ is the magnitude of the projection of the electronic angular momentum on the internuclear axis, J is the total orbital angular momentum, M is the projection of the total orbital angular momentum along the lab frame z -axis, and $\tilde{D}_{M\Lambda}^J(\phi, \theta, 0)$ is the Wigner D -function normalized over the polar and azimuthal angles θ and ϕ that describe the orientation of the molecular axis relative to the lab frame.

In order to reduce the number of electronic channels required in Eq. (6), we examine the Born-Oppenheimer potentials and dipole couplings to understand the role of electronic excitation for our parameters. From Fig. 2, we see that there is a difference of at least 0.40 a.u. in energy between the ground electronic channel $X^1\Sigma^+$ and the first excited channel $A^1\Sigma^+$. Therefore, a minimum of eight photons is required for electronic excitation with an 800 nm pulse, the shortest wavelength that we consider. Moreover, we see from Fig. 3 that the magnitudes of the permanent dipole, $\langle\Phi_1|\mathbf{d}|\Phi_1\rangle$, and the $X^1\Sigma^+-A^1\Sigma^+$ transition dipole matrix element, $\langle\Phi_1|\mathbf{d}|\Phi_2\rangle$, have nearly the same value for $1.0 \text{ a.u.} \leq R \leq 2.0 \text{ a.u.}$, and that the permanent dipole is larger for $R > 2.0 \text{ a.u.}$ In the range where the matrix elements are comparable, however, a minimum of thirteen 800 nm photons is required for electronic excitation. Taken together, these considerations suggest that electronic excitation will be negligible for all but very high intensities. Therefore, we will neglect electronic excitation in our calculations and keep only the $X^1\Sigma^+$ state. Because our calculations only involve one electronic channel, we will drop the electronic channel labels for the remainder of this work.

When our calculations were carried out, the extensive results for the dipole matrix elements in Ref. [29] had not yet been published, so we used an approximate form of the permanent dipole:

$$\langle \Phi | \mathbf{d} | \Phi \rangle = \frac{m_A}{m_A + m_B} \mathbf{R}. \quad (7)$$

This form is exact asymptotically as the system dissociates to $\text{He}(1s^2) + \text{H}^+$ and can be derived either classically or by direct evaluation in the separated atom limit. Figure 3 compares this approximate dipole to the accurately calculated ones from Ref. [29]. The figure shows our approximation to be in good agreement with the calculated dipole with discrepancies for small R . The fact that the actual dipole is smaller than the one used in our calculations implies that the intensity required to produce a given dissociation probability will be larger than found in our calculations. However, lowest order perturbation theory predicts that the actual and reported intensities required to produce the lowest energy kinetic energy release (KER) peak are of the same order of magnitude for the wavelengths considered.

With the above approximations, Eq. (6) reduces to

$$\Psi = \sum_J \frac{1}{R} F_J(R, t) Y_{J0}(\phi, \theta) \Phi(R; \mathbf{r}_1, \mathbf{r}_2), \quad (8)$$

where $\tilde{D}_{00}^J = Y_{J0}$ was used and we have assumed linearly polarized light in order to include only $M = 0$ in the expansion. Substituting this sum into Eq. (3), projecting out $\Phi Y_{J'0}$, and using Eq. (7) gives the equations we solve for the radial part of the wavefunction:

$$i \frac{\partial}{\partial t} F_J = \left[-\frac{1}{2\mu_{AB}} \frac{\partial^2}{\partial R^2} + \frac{J(J+1)}{2\mu_{AB}R^2} + U \right] F_J - \sum_{J'} \frac{m_A}{m_A + m_B} \mathcal{E}(t) R \sqrt{\frac{4\pi}{3}} \langle Y_{J0} | Y_{10} | Y_{J'0} \rangle F_{J'}, \quad (9)$$

where we have taken the laser polarization in the lab frame $\hat{\mathbf{z}}$ direction. Equation (9) neglects all coupling between electronic states, including non-Born-Oppenheimer effects and Coriolis coupling [31].

B. Numerical Methods

The remaining task is to solve Eq. (9). Time propagation of a given initial state is carried out according to Eq. (9) using the generalized finite differencing scheme from Ref. [32] to approximate the time-dependent Hamiltonian as the block tridiagonal matrix $\mathbf{H}(t)$. Here, the diagonal blocks are the matrix representation of the field-free Hamiltonian, and each off-diagonal block is a diagonal matrix with the J' to $J' \pm 1$ dipole coupling. Using $\mathbf{H}(t)$, time propagation is accomplished for small time steps δ by

$$\mathbf{F}(R, t + \delta) = e^{-i\mathbf{H}(t+\delta/2)\delta} \mathbf{F}(R, t), \quad (10)$$

where the components of \mathbf{F} are the F_J in Eq. (8). The action of this short-time propagator is carried out by applying the split-operator techniques and the Crank-Nicolson method outlined in Ref. [33].

We use initial vibrational states with $J = 0$ and express the electric field as

$$\mathcal{E} = \mathcal{E}_0 e^{-(t/\tau)^2} \cos \omega t, \quad (11)$$

where ω is the carrier frequency and $\tau = \tau_{\text{FWHM}}/\sqrt{2\ln 2}$. Our calculations are carried out for τ_{FWHM} corresponding to both five cycle and ten cycle pulses, using wavelengths in the 800–2400 nm range and intensities between 10^{12} W/cm² and 10^{14} W/cm². Calculations begin at the time t_i when the intensity of the field is 10^7 W/cm² and end at the time t_f , after the peak intensity, when the intensity falls off to 10^8 W/cm². The time step is $\delta = 0.30$ a.u., and we dynamically increase the number of partial waves included in our expansion of Ψ [6, 7], leading to a maximal expansion of between 10 and 27 partial waves depending on the parameters of the laser pulse. For five cycle pulses, we use a non-uniform radial grid with $R_{\text{min}} = 0.20$ a.u., $R_{\text{max}} = 120.0$ a.u., and a grid spacing $\Delta R \approx 0.00094$ a.u. for $0.20 \text{ a.u.} \leq R \leq 8.0 \text{ a.u.}$ and $\Delta R \approx 0.0094$ a.u. for $R > 8.0 \text{ a.u.}$ Three point averaging, where each of three adjacent grid points is weighted equally, is repeatedly applied 20,000 times to all of the grid points in order to smooth the abrupt change in grid spacing at $R=8.0$ a.u. This smoothing is necessary for a non-uniform grid to avoid a loss of accuracy in the radial derivatives of our wavefunction near $R = 8.0$ a.u. For ten cycle pulses, we use the same grid spacing but extend R_{max} to 200.0 a.u. Convergence with respect to all of these parameters was tested and found to give the KER spectrum accurate to three digits up to an energy of 0.20 a.u.

Because part of our aim is to identify the parameters that give the largest dissociation signal, we choose the isotopes of helium and hydrogen that maximize the dipole moment and, thus, the dissociation at a given intensity. Equation (7) shows that in order to maximize the dipole, we want the isotopes with the most asymmetric masses. Consequently, we consider ^4He and ^1H . For their masses, we use $m_A = 7351.67$ a.u. and $m_B = 1836.15$ a.u.

III. RESULTS AND DISCUSSION

A. Dissociation Probability

To quickly locate the parameters that produce substantial dissociation, we first consider the total dissociation probability

$$P = 1 - \sum_{vJ} |\langle \chi_{vJ} | F_J(t_f) \rangle|^2, \quad (12)$$

for a series of initial vibrational states. In Eq. (12), χ_{vJ} are the field-free ro-vibrational nuclear eigenstates and

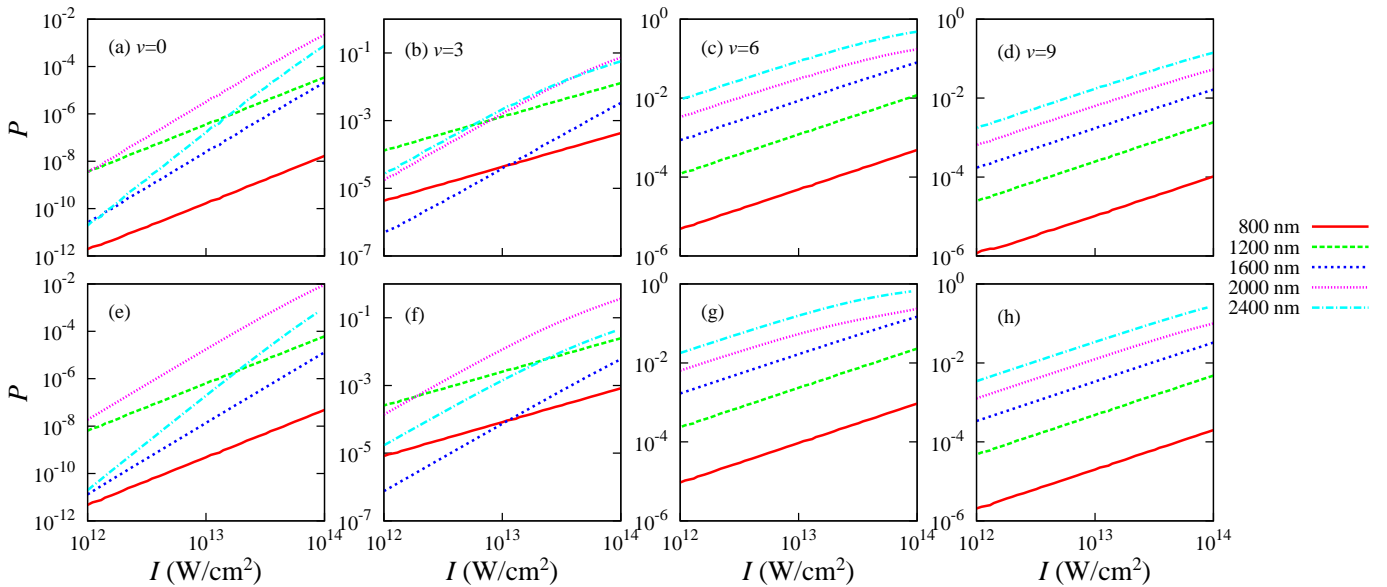


FIG. 4. (Color online.) Total dissociation probability P as a function of intensity for different wavelengths, pulse lengths, and initial vibrational states. The top figures are for 5 cycle pulses, while the bottom figures are for 10 cycle pulses. From left to right, the columns correspond to the initial vibrational states $v=0, 3, 6,$ and 9 .

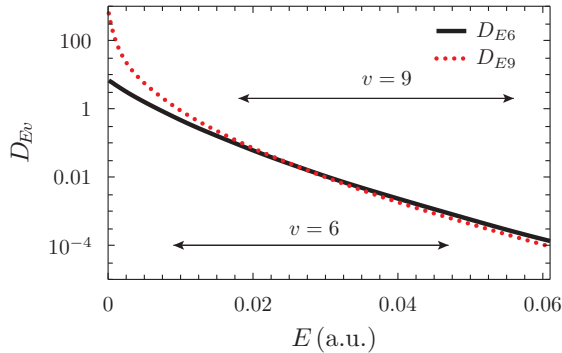


FIG. 5. (Color online.) Bound-free dipole matrix elements, Eq. (13), as a function of KER E for $v = 6$ and $v = 9$. The horizontal arrows represent the range of energies expected for one photon absorption for wavelengths between 2400 nm and 800 nm.

$F_J(t_f)$ are the components given by Eq. (9). The intensity dependence of P for several initial vibrational states is presented in Fig. 4. From the figure, we see that $P \propto I^n$ for most initial vibrational states, which is the result expected from lowest order perturbation theory for n photon absorption. Deviations from I^n do appear for high intensities, indicating that lowest order perturbation theory is no longer adequate. Figure 2 shows that for an initial $v = 0$ state, two photons are required for dissociation at 800 nm and 1200 nm, three photons are required at 1600 nm and 2000 nm, and four photons are required at 2400 nm. These values of n are consistent with the slopes found in Fig. 4. This same analysis can be applied to explain the slopes seen for other initial states in the figure.

From Fig. 4, we see that there do exist parameters that produce substantial dissociation: up to 8.5% (five cycles) and 16% (ten cycles) for 10^{13} W/cm², and up to 48% and 65% for 10^{14} W/cm², respectively. In all cases, these maximal P occurred for $v = 6$ at 2400 nm — not surprising considering only one photon is required for dissociation from this state. Dissociation from $v = 9$, however, also requires only a single photon, yet its dissociation probability is an order of magnitude smaller than for $v = 6$. The difference in dissociation probability for these two states is explained by their bound-free dipole matrix element,

$$D_{Ev} = \left\langle E, J = 1 \left| \frac{m_A}{m_A + m_B} R \right| \chi_{v0} \right\rangle, \quad (13)$$

where $|E, J\rangle$ is the the energy normalized field-free continuum state with energy E and angular momentum J . Figure 5 shows D_{E9} and D_{E6} together with the ranges of KER expected in each case for the one-photon peak for wavelengths between 2400 nm and 800 nm. Keeping in mind that the vertical scale in the figure is logarithmic, it is clear that D_{E9} is considerably smaller than D_{E6} at any given wavelength, yielding, in turn, a much smaller dissociation probability.

The wavelength dependence of P evident in Fig. 4 can also be explained by D_{Ev} . In Fig. 5, we see that for $v=6$ and 9 the dipole matrix elements decrease monotonically with increasing KER. In fact, this behavior is a general feature of D_{Ev} for this system. Therefore, longer wavelengths are expected to give the largest dissociation probabilities since they produce dissociating fragments with the lowest KER.

There is also substantial dissociation for other initial

states and laser parameters. Both five and ten cycle pulses with $I = 10^{14}$ W/cm² produce dissociation probabilities greater than 1.0% for both $\lambda = 2000$ nm and $\lambda = 2400$ nm in all studied initial vibrational states except $v = 0$. Because the largest dissociation occurs for intensities between 10^{13} W/cm² and 10^{14} W/cm² and wavelengths between 2000 nm and 2400 nm, we constrain our studies of the KER and momentum distribution to this region of parameter space.

B. Kinetic Energy Release Spectrum

Due to the fact that HeH⁺ is a benchmark molecular system, it is useful to try to understand its behavior in a laser field using the pictures already developed for the benchmark molecule H₂⁺. In particular, the dressed potentials of the Floquet representation have proven especially useful in understanding the kinetic energy release spectrum of H₂⁺ [2, 8, 15]. These dressed potentials are obtained by shifting the Born-Oppenheimer potentials by integer multiples of ω , keeping only those states connected by one or more application of the dipole selection rules. At crossings of the dressed potentials, transitions are much more likely because these crossings correspond to a resonance-like condition.

Because there is only one electronic channel relevant for our laser conditions, shifting it by multiples of ω produces parallel potentials with no crossings. When the appropriate centrifugal barriers are included, there are crossings, but only for such high J and photon number that they are not likely to produce transitions. Thus, non-resonant transitions must dominate for the laser parameters we consider, reducing the utility of the dressed potential picture in this study. We note that this failure of the dressed photon picture will be generally true for processes dominated by permanent dipole transitions and is not a feature specific to HeH⁺. If we were considering shorter wavelengths, such that transitions to the $A^1\Sigma^+$ (or higher) state were relevant, then the dressed potential picture would again prove useful.

It seems, then, that to understand the dissociation of HeH⁺, we must think about the process differently than for H₂⁺. A natural picture to adopt is that for atomic ionization because including only a single channel makes the HeH⁺ nuclear time-dependent Schrödinger equation, Eq. (9), look just like that of a hydrogenic atom. Pursuing this analogy, Eq. (9) shows that the “electron” in HeH⁺ has a charge of $m_A/(m_A + m_B)$, a mass of μ_{AB} , and interacts via a short-range central potential. This analogy allows us to interpret our results using the pictures that are used to understand intense field ionization.

Atomic ionization is primarily understood using one of two pictures: tunneling or multiphoton ionization. Which picture is most appropriate is customarily determined by the value of the Keldysh parameter $\gamma = \sqrt{E_b/2U_p}$, where E_b is the electronic binding energy and $U_p = q^2\mathcal{E}^2/4\mu\omega^2$ is the ponderomotive energy [34, 35]. In

the case of ionization, the charge q and mass μ in U_p refer to an electron and are unity in atomic units. However, for our analog system, where we are concerned with a nuclear Keldysh parameter rather than an electronic one, these values change substantially: E_b becomes the dissociation energy for a given initial ro-vibrational state, the reduced mass is 1469.20 a.u., and the “charge” is 0.80 a.u. Like the electronic Keldysh parameter, the value of our nuclear Keldysh parameter tells us whether our system is in the multiphoton or tunneling dissociation regime.

For HeH⁺($v=3, J=0$) in a 2400 nm laser pulse with peak intensity $I=8.9\times 10^{13}$ W/cm², $\gamma = 4.6$, placing the system in the multiphoton regime. For higher-lying ro-vibrational states, the Keldysh parameter will become smaller at these laser parameters, dropping to $\gamma=0.67$ for HeH⁺($v=9, J=0$). So, with relatively modest — and likely achievable — changes in the laser parameters, HeH⁺ can be studied over the whole range of physical regimes from multiphoton to tunneling. For the remainder of this paper, however, we will restrict our consideration to HeH⁺($v=3, J=0$) in a 2400 nm pulse with $I=8.9\times 10^{13}$ W/cm² which lies in the multiphoton regime. Consequently, we expect to see many of the same phenomena that are seen in the multiphoton ionization of atoms, such as above threshold ionization (ATI), in the strong-field dissociation of HeH⁺.

One commonly studied observable in atomic systems that reveals these phenomena is the photoelectron spectrum. In HeH⁺, the analog is the KER spectrum. That is, the probability of the molecule dissociating with a relative nuclear kinetic energy E ,

$$\frac{dP}{dE} = \sum_J |\langle E, J | F_J(t_f) \rangle|^2. \quad (14)$$

A typical result for the KER spectrum in the parameter space that we are considering is shown in Fig. 6. This spectrum clearly shows the characteristic photon-spaced peaks expected for above threshold ionization (ATI) — except, of course, that this is the nuclear KER spectrum, making it above threshold dissociation (ATD). In the atomic case, the energies of the ATI peaks are given by $E_n = n\omega - E_b - U_p$, where n is the net number of photons absorbed. Because the ponderomotive energy is negligible for the parameters we are considering ($U_p/\omega = 0.040$ for the parameters in Fig. 6 and Fig. 7), this result simplifies to $E_n/\omega = E_b/\omega + n$. For $v = 3$ and $\lambda = 2400$ nm, we expect the first peak to occur for two photon absorption at $E_{n=2}/\omega = 0.26$, which is in good agreement with the result in Fig. 6.

It is also important to note the large number of ATD peaks visible in Fig. 6. Our result shows more ATD orders than is typical and is a consequence of the large energy difference between the $X^1\Sigma^+$ and $A^1\Sigma^+$ potentials, which allows for the absorption of many photons before electronic excitation plays a role and blurs the peaks. Even so, the highest ATD peak shown in Fig. 6 lies 0.19 a.u. — more than eleven photons — below the minimum of the $A^1\Sigma^+$ potential.

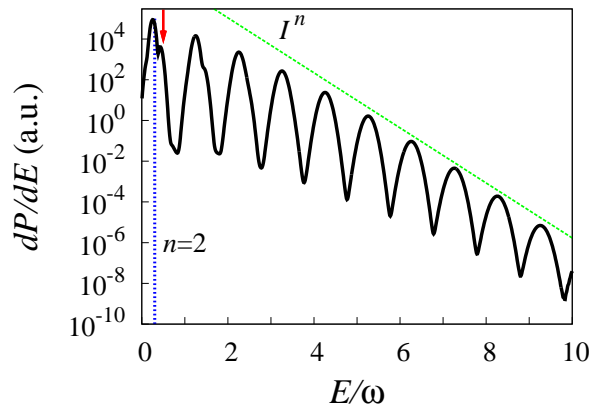


FIG. 6. (Color online.) The KER spectrum for an initial vibrational state of $v = 3$ in a five cycle pulse. The vertical dashed line at $E/\omega = 0.26$ corresponds to the expected location of the first peak, and the dashed diagonal line shows the $dP/dE \propto I^n$ behavior expected from lowest-order perturbation theory.

One notable difference between Fig. 6 and a typical ATI spectrum is the absence of the plateau usually seen for $3.17U_p < E < 10U_p$ [34]. Because the ponderomotive energy is small relative to the frequency of the laser, our ATD plateau would occur between $E/\omega = 0.13$ and $E/\omega = 0.40$. The fact that $10U_p/\omega - 3.17U_p/\omega$ is much smaller than one explains our inability to observe an ATD plateau. Physically, this small interval is due to the fact that the massive nuclei are unable to gain a substantial amount of energy in the field. For a pulse with $I = 8.9 \times 10^{13} \text{ W/cm}^2$, it would require a wavelength of almost $3.7 \mu\text{m}$ to produce a plateau region with a large enough energy range to fit two KER peaks.

Finally, the spectrum in Fig. 6 shows that high-order, non-linear processes are occurring: the figure gives evidence for at least eleven photon absorption. Nevertheless, Fig. 4(b) suggests that the deviation from lowest-order perturbation theory is small. This apparent inconsistency can be reconciled by recognizing that the area under the $n = 2$ peak dominates the energy integral needed to calculate dissociation probability from dP/dE . However, Fig. 6 also shows that the non-perturbative effects extend beyond the presence of high-order ATD peaks. The diagonal line indicates I^n behavior that matches the highest energy peaks as expected. The lower peaks, however, do not meet this line, suggesting the contribution of high-order pathways in these peaks. Due to their dominating the energy integral of dP/dE , it is this deviation from I^n that produces the non-perturbative behavior seen in Fig. 4(b) rather than the presence of the higher-order peaks.

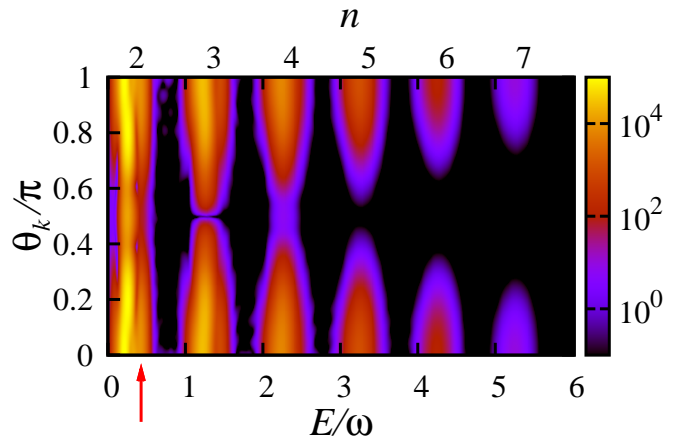


FIG. 7. (Color online.) “Momentum” distribution from Eq. (15) plotted as a function of KER E and angle θ_k for an initial ro-vibrational state with $v=3$ and $J=0$ in a five cycle pulse with an intensity of $8.9 \times 10^{13} \text{ W/cm}^2$ and a wavelength of 2400 nm. The upper-axis label n indicates the net number of photons absorbed.

C. Momentum Distribution

We can also use the atomic analogy to understand the distribution of relative nuclear momenta \mathbf{k}

$$\frac{\partial^2 P}{\partial E \partial \theta_k} = 2\pi |\langle \mathbf{k} | \Psi(t_f) \rangle|^2, \quad (15)$$

where θ_k is the scattering angle with respect to the laser polarization and the state $|\mathbf{k}\rangle$ is an energy-normalized scattering state with asymptotic out-going momentum \mathbf{k} . Note that Eq. (14) is obtained from Eq. (15) by integrating over the angle θ_k . The momentum distribution for $v = 3$ and $\lambda = 2400 \text{ nm}$, the same case shown in Fig. 6, is shown in Fig. 7. We, of course, still see the photon-spaced peaks with decreasing probability, as expected from the atomic ionization picture and Fig. 6. The angular distribution of each ATD peak is consistent with the identification of the number of photons involved. For instance, the peaks at $E/\omega = 0.3, 2.3, \dots$ are nonzero at $\theta_k/\pi = 0.50$ as expected for even parity final states produced by the absorption of $n = 2, 4, \dots$ photons from the $J = 0$ initial state. Similarly, the peaks at $E/\omega = 1.3, 3.3, \dots$ have a node at $\theta_k/\pi = 0.50$ corresponding to an odd number of photons absorbed — specifically, $n = 3, 5, \dots$ — from the $J = 0$ initial state.

In both Fig. 6 and Fig. 7, there is additional structure on the two-photon peak in the form of a peak at $E/\omega = 0.50$ (indicated by arrows in the figures). This peak can be explained by noting that the $v = 3$ to $v = 6$ transition is nearly on resonance for 2400 nm: $\omega_{63} = 1.2\omega$. Even though the effective intensity at ω_{63} is reduced by seven orders of magnitude, the resonant enhancement is still sufficient to produce a peak. Moreover, this resonance enhanced multiphoton dissociation (REMPD) mechanism correctly predicts the peak to be

at $E/\omega = 0.50$ in agreement with our calculations. A REMPDP peak is noticeable on the $n = 3$ peaks in the figures as well. For higher order peaks, however, the REMPDP peak grows increasingly broad in energy due to the bandwidth of the laser pulse, washing it out as a distinct peak. As its name suggests, REMPDP is the analog of the well-known resonance enhanced multiphoton ionization in ATI spectra [35], and we expect it to be ubiquitous in long wavelength dissociation of HeH^+ since these wavelengths are more likely to drive a bound-bound resonance.

IV. SUMMARY AND OUTLOOK

We have proposed HeH^+ as a benchmark system for understanding the nuclear dynamics of heteronuclear molecules in intense laser fields. However, given that dissociation of HeH^+ at the common intense laser wavelength of 800 nm is consistently below useful experimental detection levels at intensities that will not also ionize the molecule, it was necessary to explore other laser parameters. We find that increasing the wavelength is an effective way to increase the dissociation probability at modest intensities. In particular, for wavelengths between 2000 nm and 2400 nm and intensities between 10^{13} W/cm² and 10^{14} W/cm², we see probabilities greater than one percent for $v = 3, 6, \text{ and } 9$, making dissociation of HeH^+ experimentally accessible. In general, we expect even larger HeH^+ dissociation probabilities for wavelengths longer than the 2400 nm considered here.

It turns out that HeH^+ is a rather unique molecule in that the minimum electronic excitation energy is relatively large. While this property decreases its utility as a prototype for the behavior of heteronuclear molecules generally, it does allow for the surprising possibility of understanding the nuclear dynamics of HeH^+ in terms of atomic ionization pictures. The same reduction of the system to a single channel also has the intriguing conse-

quence that all of the nuclear dynamics for a substantial range of laser parameters is induced by the molecule's permanent dipole. This lies in contrast to the electronic transition dominated strong-field response of most every other molecule that has been studied to date.

So, while HeH^+ may not be the general prototype we aimed for, it is still a very interesting molecule to study. Even though much of the physics for this system can be understood using atomic pictures, HeH^+ still exhibits molecular behavior that differentiates it from the atomic systems that have been studied in the past. As a molecule, for example, the initial state of the system will actually be an incoherent distribution of ro-vibrational states determined by the temperature and mechanism for creation of the molecule — unlike atoms. The strong-field dynamics of HeH^+ is thus not exactly molecule-like, and it is not exactly atom-like. But, with only two electrons, it *is* a benchmark system for which precision calculations and experiments ought to be possible to elucidate the dynamics of a system that displays physical behavior in limbo between that of molecule and that of an atom.

ACKNOWLEDGMENTS

We are grateful for many useful discussions with I. Ben-Itzhak, who provided the initial suggestion that we study HeH^+ and gave much insight on its experimental accessibility. We are also grateful for many useful discussions with his group. In addition, we wish to thank N. Vaeck and the other authors of Ref. [29], who sent us their numerical data for the dipole matrix elements of HeH^+ . The authors acknowledge support the Chemical Sciences, Geosciences, and Biosciences Division, Office of Basic Energy Sciences, Office of Science, US Department of Energy. DU further acknowledges support from the National Science Foundation (Grant Number PHY-0552878) during the early stages of this work.

-
- [1] A. Giusti-Suzor, F. H. Mies, L. F. DiMauro, E. Charron, and B. Yang, *J. Phys. B* **28**, 309 (1995).
 - [2] J. H. Posthumus, *Rep. Prog. Phys.* **67**, 623 (2004).
 - [3] I. V. Hertel and W. Radloff, *Rep. Prog. Phys.* **69**, 1897 (2006)
 - [4] C. R. Calvert, W. A. Bryan, W. R. Newell and I. D. Williams, *Phys. Rep.* **491**, 1 (2010).
 - [5] V. N. Serov, A. Keller, O. Atabek, and N. Billy, *Phys. Rev. A* **68**, 053401 (2003).
 - [6] V. Serov, A. Keller, O. Atabek, H. Figger, and D. Pavicic, *Phys. Rev. A* **72**, 033413 (2005).
 - [7] I. Ben-Itzhak, A. M. Saylor, P. Q. Wang, J. McKenna, B. Gaire, N. G. Johnson, M. Leonard, E. Parke, K. D. Carnes, F. Anis, and B. D. Esry, *J. Phys.: Conf. Ser.* **88**, 012046 (2007).
 - [8] F. Anis and B. D. Esry, *Phys. Rev. A* **77**, 033416 (2008).
 - [9] J. McKenna, A. M. Saylor, F. Anis, B. Gaire, N. G. Johnson, E. Parke, J. J. Hua, H. Mashiko, C. M. Nakamura, E. Moon, Z. Chang, K. D. Carnes, B. D. Esry, and I. Ben-Itzhak, *Phys. Rev. Lett.* **100**, 133001 (2008).
 - [10] F. Anis, T. Cackowski, and B. D. Esry, *J. Phys. B* **42**, 091001(FTC) (2009).
 - [11] J. McKenna, F. Anis, B. Gaire, N. G. Johnson, M. Zohrabi, K. D. Carnes, B. D. Esry, and I. Ben-Itzhak, *Phys. Rev. Lett.* **103**, 103006 (2009).
 - [12] A. Giusti-Suzor, X. He, O. Atabek, and F. H. Mies, *Phys. Rev. Lett.* **64**, 515 (1990).
 - [13] L. J. Frasinski, J. H. Posthumus, J. Plumridge, K. Codling, P. F. Taday, and A. J. Langley, *Phys. Rev. Lett.* **83**, 3625 (1999).
 - [14] V. Roudnev, B. D. Esry, and I. Ben-Itzhak, *Phys. Rev. Lett.* **93**, 163601 (2004).
 - [15] J. J. Hua and B. D. Esry, *J. Phys. B* **42**, 085601 (2009).
 - [16] M. F. Kling, C. Siedschlag, A. J. Verhoef, J. I. Khan, M.

- Schultze, T. Uphues, Y. Ni, M. Uiberacker, M. Drescher, F. Krausz, and M. J. J. Vrakking, *Science* **312**, 246 (2006).
- [17] E. Charron, A. Giusti-Suzor, and F. H. Mies, *Phys. Rev. Lett.* **75**, 2815 (1995).
- [18] B. Sheehy, B. Walker, and L. F. DiMauro, *Phys. Rev. Lett.* **74**, 4799 (1995).
- [19] D. Ray, F. He, S. De, W. Cao, H. Mashiko, P. Ranitovic, K. P. Singh, I. Znakovskaya, U. Thumm, G. G. Paulus, M. F. Kling, I. V. Litvinyuk, and C. L. Cocke, *Phys. Rev. Lett.* **103**, 223201 (2009).
- [20] P. H. Bucksbaum, A. Zavriyev, H. G. Muller, and D. W. Schumacher, *Phys. Rev. Lett.* **64**, 1883 (1990).
- [21] A. Zavriyev, P. H. Bucksbaum, J. Squier, and F. Saline, *Phys. Rev. Lett.* **70**, 1077 (1993).
- [22] P. Q. Wang, A. M. Sayler, K. D. Carnes, J. F. Xia, M. A. Smith, B. D. Esry, and I. Ben-Itzhak, *J. Phys. B* **38**, L251 (2005).
- [23] I. Ben-Itzhak, I. Gertner, O. Heber, and B. Rosner, *Phys. Rev. Lett.* **71**, 1347 (1993).
- [24] I. Ben-Itzhak, Z. Chen, B.D. Esry, I. Gertner, O. Heber, C.D. Lin, and B. Rosner, *Phys. Rev. A* **49**, 1774 (1994).
- [25] H.B. Pedersen, S. Altevogt, B. Jordon-Thaden, O. Heber, M. L. Rappaport, D. Schwalm, J. Ullrich, D. Zajfman, R. Treusch, N. Guerassimova, M.Martins, J.-T. Hoeft, M. Wellhöfer, A. Wolf, *Phys. Rev. Lett.* **98**, 223202 (2007).
- [26] P. Colosimo, G. Doumy, C.I. Blaga, J. Wheeler, C. Hauri, F. Catoire, J. Tate, R. Chirla, A. M. March, G. G. Paulus, H. G. Muller, P. Agostini, and L. F. DiMauro, *Nature Phys.* **4**, 386 (2008).
- [27] C.I. Blaga, F. Catoire, P. Colosimo, G. G. Paulus, H. G. Muller, P. Agostini, L. F. DiMauro, *Nature Phys.* **5**, 335 (2009).
- [28] B. Bergues, S. Zherebtsov, Y. Deng, X. Gu, I. Znakovskaya, R. Kienberger, F. Krausz, G. Marcus, M.F. Kling, *New J. Phys.* **13**, 063010 (2011).
- [29] J. Loreau, J. Liévin, P. Palmeri, P. Quinet, and N. Vaeck, *J. Phys. B* **43**, 065101 (2010).
- [30] W. Kolos and J. Peek, *Chem. Phys.* **12**, 381 (1976).
- [31] R. Pack and J. Hirschfelder, *J. Chem. Phys.* **49**, 4009 (1968).
- [32] M. W. J. Bromley and B. D. Esry, *Phys. Rev. A* **69**, 053620 (2004).
- [33] P. Q. Wang, A. M. Sayler, K. D. Carnes, J. F. Xia, M. A. Smith, B. D. Esry, and I. Ben-Itzhak, *Phys. Rev. A* **74**, 043411 (2006).
- [34] W. Becker, F. Grasbon, R. Kopold, D. Milošević, G. Paulus, and H. Walther, *Adv. At. Mol. Opt. Phys.* **48**, 35 (2002).
- [35] B. Bransden and C. Joachain, *Physics of Atoms and Molecules 2nd Edition* (Pearson Education London, Harlow, England, 2003).